

## A GROUND-BASED OPTICAL TRANSMISSION SPECTRUM OF WASP-6b

ANDRÉS JORDÁN<sup>1</sup>, NÉSTOR ESPINOZA<sup>1</sup>, MARKUS RABUS<sup>1</sup>, SUSANA EYHERAMENDY<sup>2</sup>, DAVID K. SING<sup>3</sup>,  
JEAN-MICHEL DÉSSERT<sup>4,5</sup>, GÁSPÁR Á. BAKOS<sup>6,11,12</sup>, JONATHAN J. FORTNEY<sup>7</sup>, MERCEDES LÓPEZ-MORALES<sup>8</sup>,  
PIERRE F. L. MAXTED<sup>9</sup>, AMAURY H. M. J. TRIAUD<sup>10,13</sup>, AND ANDREW SZENTGYORGYI<sup>8</sup>

<sup>1</sup> Instituto de Astrofísica, Facultad de Física, Pontificia Universidad Católica de Chile, Av. Vicuña Mackenna 4860, 7820436 Macul, Santiago, Chile

<sup>2</sup> Departamento de Estadística, Facultad de Matemáticas, Pontificia Universidad Católica de Chile, Av. Vicuña Mackenna 4860, 7820436 Macul, Santiago, Chile  
<sup>3</sup> School of Physics, University of Exeter, Stocker Road, Exeter EX4 4QL, UK

<sup>4</sup> CASA, Department of Astrophysical and Planetary Sciences, University of Colorado, Boulder, CO 80309, USA

<sup>5</sup> Division of Geological and Planetary Sciences, California Institute of Technology, MC 170-25 1200, East California Boulevard, Pasadena, CA 91125, USA

<sup>6</sup> Department of Astrophysical Sciences, Princeton University, Princeton, NJ 08544, USA

<sup>7</sup> Department of Astronomy and Astrophysics, University of California, Santa Cruz, CA 95064, USA

<sup>8</sup> Harvard-Smithsonian Center for Astrophysics, 60 Garden Street, Cambridge, MA 02138, USA

<sup>9</sup> Astrophysics Group, Keele University, Staffordshire ST5 5BG, UK

<sup>10</sup> Department of Physics, and Kavli Institute for Astrophysics and Space Research, Massachusetts Institute of Technology, Cambridge, MA 02139, USA

Received 2013 September 29; accepted 2013 October 21; published 2013 November 13

### ABSTRACT

We present a ground-based optical transmission spectrum of the inflated sub-Jupiter-mass planet WASP-6b. The spectrum was measured in 20 spectral channels from 480 nm to 860 nm using a series of 91 spectra over a complete transit event. The observations were carried out using multi-object differential spectrophotometry with the Inamori-Magellan Areal Camera and Spectrograph on the Baade Telescope at Las Campanas Observatory. We model systematic effects on the observed light curves using principal component analysis on the comparison stars and allow for the presence of short and long memory correlation structure in our Monte Carlo Markov Chain analysis of the transit light curves for WASP-6. The measured transmission spectrum presents a general trend of decreasing apparent planetary size with wavelength and lacks evidence for broad spectral features of Na and K predicted by clear atmosphere models. The spectrum is consistent with that expected for scattering that is more efficient in the blue, as could be caused by hazes or condensates in the atmosphere of WASP-6b. WASP-6b therefore appears to be yet another massive exoplanet with evidence for a mostly featureless transmission spectrum, underscoring the importance that hazes and condensates can have in determining the transmission spectra of exoplanets.

*Key words:* planetary systems – planets and satellites: atmospheres – techniques: spectroscopic

*Online-only material:* color figures

### 1. INTRODUCTION

Due to their fortuitous geometry, transiting exoplanets allow the determination of physical properties that are inaccessible or hard to reach for non-transiting systems. One of the most exciting possibilities enabled by the transiting geometry is to measure atmospheric properties of exoplanets without the need to resolve them from their parent star through the technique of transmission spectroscopy. In this technique, the atmospheric opacity at the planet terminator is probed by measuring the planetary size via transit light-curve observations at different wavelengths. The measurable quantity is the planet-to-star radius ratio as a function of wavelength,  $(R_p/R_*) (\lambda) \equiv k(\lambda)$ , and is termed the transmission spectrum. The measurement of a transmission spectrum is a challenging one, with one atmospheric scale height  $H$  translating to a signal of order  $2Hk \approx 10^{-4}$  for hot Jupiters (e.g., Brown 2001). The requirements on precision favor exoplanets with large atmospheric scale heights, large values of  $k$  (e.g., systems transiting M dwarfs), and orbiting bright targets due to the necessity of acquiring a large number of photons to reach the needed precision.

The first successful measurement by transmission spectroscopy was the detection with the *Hubble Space Telescope*

(*HST*) of absorption by NaI in the hot Jupiter HD 209458b (Charbonneau et al. 2002). The signature of Na was 2–3 times weaker than expected from clear atmosphere models, providing the first indications that condensates can play an important role in determining the opacity of their atmospheres as seen in transmission (e.g., Fortney 2005, and references therein). Subsequent space-based studies have concentrated largely on the planets orbiting the stars HD 209458 and HD 189733 due to the fact that they are very bright stars and therefore allow the collection of a large number of photons even with the modest aperture of space-based telescopes. A recent study of all the transmission spectra available for HD 189733, spanning the range from 0.32 to 24  $\mu\text{m}$ , points to a spectrum dominated by Rayleigh scattering over the visible and near-infrared range, with the only detected feature being a narrow resonance line of Na (Pont et al. 2013). For HD 209458, Deming et al. (2013) present new WFC3 data combined with previous Space Telescope Imaging Spectrograph data (Sing et al. 2008), resulting in a transmission spectrum spanning the wavelength range 0.3–1.6  $\mu\text{m}$ . They conclude that the broad features of the spectrum are dominated by haze and/or dust opacity. In both cases the spectra are different from those predicted by clear atmosphere models that do not incorporate condensates.

In order to further our understanding of gas giant atmospheres, it is necessary to build a larger sample of systems with measured transmission spectra. Hundreds of transiting exoplanets, mostly hot gas giants, have been discovered by ground-based

<sup>11</sup> Alfred P. Sloan Fellow.

<sup>12</sup> Packard Fellow.

<sup>13</sup> Fellow of the Swiss National Science Foundation.

**Table 1**  
List of Comparison Stars

2MASS Identifier
2MASS-23124095-2243232
2MASS-23124836-2252099
2MASS-23124448-2253190
2MASS-23124428-2256403
2MASS-23114068-2248130
2MASS-23113937-2250334
2MASS-23114820-2256592

surveys such as HATNet (Bakos et al. 2004), WASP (Pollacco et al. 2006), KELT (Pepper et al. 2007), XO (McCullough et al. 2005), TRES (Alonso et al. 2004), and HATSouth (Bakos et al. 2013), with magnitudes within reach of the larger collecting areas afforded by ground-based telescopes but often too faint for *HST*.<sup>14</sup> The ground-based observations have to contend with the atmosphere and instruments lacking the space-based stability of *HST*, but despite these extra hurdles the pace of ground-based transmission spectra studies is steadily increasing. Following the ground-based detection of Na I in HD 189733b (Redfield et al. 2008) and confirmation of Na I in HD 209358b (Snellen et al. 2008), Na I has been additionally reported from the ground in WASP-17b (Wood et al. 2011; Zhou & Bayliss 2012) and XO-2b (Sing et al. 2012). K I has been detected in XO-2b (Sing et al. 2011a) and the highly eccentric exoplanet HD 80606b (Colón et al. 2012). All of these studies have used high-resolution spectroscopy or narrowband photometry to specifically target resonant lines of alkali elements. Recently, a detection of H $\alpha$  has been reported from the ground for HD 189733b (Jensen et al. 2012), complementing previous space-based detection of Ly $\alpha$  and atomic lines in the UV with *HST* for HD 189733b and HD 209358b (Vidal-Madjar et al. 2003, 2004; Lecavelier Des Etangs et al. 2010).

Differential spectrophotometry using multi-object spectrographs offers an attractive means to obtain transmission spectra given the possibility of using comparison stars to account for the various systematic effects that affect the spectral time series obtained. Using such spectrographs, transmission spectra in the optical have been obtained for GJ 1214b (Bean et al. 2011; 610–1000 nm with VLT/FORS) and recently for WASP29-b (Gibson et al. 2013; 515–720 nm with Gemini/GMOS), with both studies finding featureless spectra. In the near-infrared Bean et al. (2013) present a transmission spectrum in the range 1.25–2.35  $\mu\text{m}$  for WASP-19b, using MMIRS on Magellan. In this work we present an optical transmission spectrum of another planet, WASP-6b, an inflated sub-Jupiter-mass ( $0.504 M_J$ ) planet orbiting a  $V = 11.9$  G dwarf (Gillon et al. 2009), in the range 471–863 nm.

## 2. OBSERVATIONS

The transmission spectrum of WASP-6b was obtained performing multi-object differential spectrophotometry with the Inamori-Magellan Areal Camera and Spectrograph (IMACS; Dressler et al. 2011) mounted on the 6.5 m Baade telescope at Las Campanas Observatory. A series of 91 spectra of WASP-6 and a set of comparison stars were obtained during a transit of the hot Jupiter WASP-6b in 2010 October 3 with the

<sup>14</sup> The *Kepler* mission (Borucki et al. 2010) has discovered thousands of transiting exoplanet candidates, but the magnitudes of the hosts are usually significantly fainter than the systems discovered by ground-based surveys, making detection of their atmospheres more challenging.

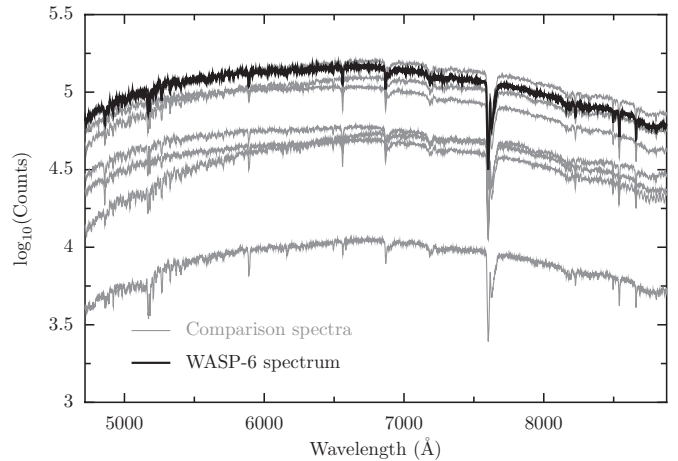


**Figure 1.** Extracted spectra for WASP-6 and the seven comparison stars used in this work for a typical exposure.

$f/2$  camera of IMACS, which provides an unvignetted circular field of view of radius  $r \approx 12$  arcmin. The large field of view makes IMACS a very attractive instrument for multi-object differential spectrophotometry as it allows us to search for suitable comparison stars that have as much as possible similar magnitude and colors as the target star. The median cadence of our observations was 224 s, and the exposure time was set to 140 s, except for the first eight exposures when we were tuning the exposure level and whose exposure times were {30, 120, 150, 150, 150, 130, 130, 130} s. The count level of the brightest pixel in the spectrum of WASP-6 was  $\approx 43,000$  ADU, i.e.,  $\approx 65\%$  of the saturation level. In addition to WASP-6, we observed 10 comparison stars of comparable magnitude, seven of which had the whole wavelength range of interest ( $\approx 4700$ – $8600$  Å) recorded in the CCD with enough signal-to-noise ratio. The seven comparison stars we used are listed in Table 1. The integrated counts over the wavelength range of interest for the spectrum of WASP-6 were typically  $\approx 3.6 \times 10^8$  electrons, giving a Poisson noise limit for the white-light light curve of  $\approx 0.06$  mmag. Each star was observed through a  $10 \times 10$  arcsec<sup>2</sup> slit in order to avoid the adverse effects of variable slit losses. We used the 300-I+17 grating as dispersing element, which gave us a seeing-dependent resolution  $\Delta\lambda$  that was  $\approx 5$  Å under 0.7 arcsec seeing and a dispersion of  $1.34$  Å pixel<sup>-1</sup>. In addition to the science mask, we obtained HeNeAr arc lamps through a mask that had slits at the same position as the science mask but with slit widths in the spectral direction of 0.7 arcsec. Observing such masks is necessary in order to produce well-defined lines that are then used to define the wavelength solution.

The extracted spectra of WASP-6 and the seven comparison stars we used are shown for a typical exposure in Figure 1. The conditions throughout the night were variable. The raw light curves constructed with the integrated counts over the whole spectral range for WASP-6 and the comparison stars are shown as a function of time in Figure 2. Besides the variation due to varying airmass (and the transit for WASP-6), there were periods with strongly varying levels of transparency concentrated in the period of time 0–2 hr after mid-transit. The seeing was in the range  $\approx 0.6$ – $0.8$ . In order to maintain good sampling of the point-spread function in the spatial direction, we defocused the telescope slightly in the periods of best seeing. Changes in seeing and transparency left no noticeable traces in the final light curves.

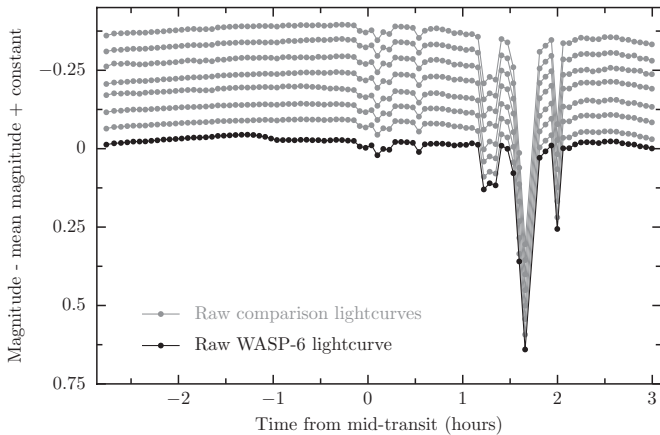


**Figure 2.** Raw light curves for WASP-6 and seven comparison stars used in this work as a function of time.

### 3. DATA REDUCTION

#### 3.1. Background and Sky Subtraction

After subtracting the median value of the overscan region to every image, an initial trace of each spectrum was obtained by calculating the centroid of each row, which are perpendicular to the dispersion direction. Each row was then divided into three regions: a central region, which contains the bulk of the light of the star; a middle, on-slit region, which is dominated by sky continuum and line emission; and an outer, out-of-slit region, which contains a smooth background outside the slit arising from, e.g., scattered light. The middle and outer regions have components on each side of the spectrum. The outermost region was used to determine a smooth background that varies slowly along the dispersion direction. The median level was obtained in the outer regions on either side of the slit, and then a third-order polynomial was used to estimate the average background level as a function of pixel in the dispersion direction. This smooth background component was then subtracted from the central and middle regions. Then a Moffat function plus a constant level  $c_i$  was fit robustly to each background-subtracted row in those regions. The estimated  $c_i$  (one per row) was then subtracted from the central and middle regions in order to obtain a spectrum where only the stellar contribution remains. It is necessary to estimate the sky emission on a row-per-row basis as sky emission lines have a wide, box-shaped form with sharp boundaries due to the fact that they fully illuminate the wide slit.

#### 3.2. Fine Tracing and Spectrum Extraction

The background- and sky-subtracted spectrum was traced by an algorithm that cross-correlates each slice perpendicular to the wavelength direction with a Gaussian in order to find the spectral trace. The centers of the trace were then fitted robustly with a fourth-order polynomial. This new tracing procedure served as a double check for the centers obtained via the centroid method in the background and sky subtraction part of the data reduction process; both methods gave traces consistent with each other. With the trace in hand, the spectrum was extracted by using a simple extraction procedure, i.e., summing the flux on each row  $\pm 15$  pixels from the trace position at that row. We also tried optimal extraction (Marsh 1989), but it led to additional

systematic effects when analyzing the light curves,<sup>15</sup> and in any case optimal extraction is not expected to give significant gains over simple extraction at the high signal-to-noise levels we are working with here. We also took spectroscopic flats at the beginning of the night with a quartz lamp and reduced the data using both flat-fielded and non-flat-fielded spectra. The results were consistent when using both alternate reductions, but the flat-fielded spectra showed higher dispersion in the final transmission spectrum. We therefore used the non-flat-fielded spectra in the present work.

#### 3.3. Wavelength Calibration

The extracted spectra were calibrated using NeHeAr lamps taken at the start of the night. The wavelength solution was obtained by the following iterative procedure: pixel centers of lines with known wavelengths were obtained by fitting Gaussians to them, and then all the pixel centers, along with the known wavelengths of the lines, were fitted by a sixth-order Chebyshev polynomial. We checked the absolute deviation of each line from the fit and removed the most deviant one from our sample, repeating the fit without it. This process was iterated, removing one line at a time, until an rms of less than  $2000 \text{ m s}^{-1}$  was obtained. The rms of the final wavelength solution was  $\approx 1200 \text{ m s}^{-1}$ , using 27 lines.

The procedure explained in the preceding paragraph served to wavelength-calibrate the first spectrum of the night closest in time to the NeHeAr lamps. In order to measure and correct for wavelength shifts throughout the night, the first spectrum was cross-correlated with the subsequent ones in pixel-space in order to find the shifts in wavelength-space. If  $\lambda_{t_0,s}(p)$  is the wavelength solution at time  $t_0$  (the beginning of the night) for star  $s$  as a function of the pixel  $p$ , then the wavelength solution at time  $t$  is just  $\lambda_{t,s}(p + \delta p_{t,s})$ , where  $\delta p_{t,s}$  is the shift in pixel-space found by cross-correlating the spectrum of star  $s$  taken at time  $t_0$  with the one taken at time  $t$ . Finally, each spectrum was fitted with a b-spline in order to interpolate each of the spectra into a common wavelength grid with pixel size  $0.75 \text{ \AA}$ .

### 4. MODELING FRAMEWORK

The observed signal of WASP-6 is perturbed with respect to its intrinsic shape, which we assume ideally to be a constant flux,  $F$ . This constant flux is multiplied by the transit signal,  $f(t; \theta)$ , which we describe parametrically using the formalism of Mandel & Agol (2002). In what follows  $\theta$  represents the vector of transit parameters. The largest departure from this idealized model in our observations will be given by systematic effects arising from atmospheric and instrumental effects, which are assumed to act multiplicatively on our signals. We will model the logarithm of the observed flux,  $L(t)$ , as

$$L(t; \theta) = S(t) + \log_{10} f(t; \theta) + \log_{10} F + \epsilon(t), \quad (1)$$

where  $S(t)$  represents the (multiplicative) perturbation to the star's flux, which we will refer to in what follows as the perturbation signal, and  $\epsilon(t)$  is a stochastic signal that represents the noise in our measurements (under the term noise we will also include potential variations of the star that are not accounted for in the estimate of the deterministic  $S(t)$  and that can be modeled by a stochastic signal).

<sup>15</sup> Optimal extraction assumes that the profile along the wavelength direction is smooth enough to be approximated by a low-order polynomial. However, this assumption is not always valid. In particular, we found that fringing in the reddest part of the spectra induces fluctuations in the extracted flux with wavelength due to the inadequacy of the smoothness assumption.

#### 4.1. Modeling the Perturbation Signal

##### 4.1.1. Estimation of Systematic Effects via Principal Component Analysis of the Comparison Stars

Each star in the field is affected by a different perturbation signal. However, these perturbation signals have in common that they arise from the same physical and instrumental sources. In terms of information, this is something we want to take advantage of. We model this by assuming that a given perturbation signal is in fact a linear combination of a set of signals  $s_i(t)$ , which represent the different instrumental and atmospheric effects affecting all of our light curves, i.e.,

$$S_k(t) = \sum_{i=1}^K \alpha_{k,i} s_i(t). \quad (2)$$

Note that this model for the perturbation signal so far includes the popular linear and polynomial trends (e.g.,  $s_i(t) = t^i$ ). According to this model, the logarithm of the flux of each of  $N$  stars without a transiting planet in our field can be modeled as

$$L_k(t; \alpha) = S_k(t; \alpha) + \log_{10} F_k + \epsilon_k(t), \quad (3)$$

where  $\alpha$  denotes the set of parameters  $\{\alpha_{k,i}\}_{i=1}^K$ . In the case in which we have a set of comparison stars, we can see each of them as an independent (noisy) measurement of a linear combination of the signals  $s_i(t)$  in Equation (2). A way of obtaining those signals is by assuming that the  $s_i(t)$  are uncorrelated random variables, in which case these signals are easily estimated by performing a principal component analysis (PCA) of the mean-subtracted light curves of the comparison stars. Given  $N$  comparison stars, one can estimate at most  $N$  components, and thus we must have  $K \leq N$ . As written in Equation (3), we cannot separate  $s_i(t)$  from  $\epsilon_k(t)$ , and in general the principal components will have contributions from both terms. If  $s_i(t) \gg \epsilon_k(t)$ , the  $K$  principal components that contribute most to the signal variance will be dominated by the perturbation signals, but some projection of the  $\epsilon_k$  into the estimates of  $s_i$  is to be expected.

##### 4.1.2. Selecting the Number of Principal Components

In our case, the number of components  $K$  is unknown a priori. We need therefore to determine an optimal number of principal components to describe the perturbation signal, taking into consideration that there is noise present in the light curves of the comparison stars and, thus, some of the principal components obtained are mostly noise. There are several possibilities for doing this depending on what we define as optimal. We will determine the optimal number of components as the minimum number of components that are able to achieve the best predictive power allowed by the maximum set of  $N$  components available.

As a measure of predictive power we use a  $k$ -fold cross-validation procedure (Hastie et al. 2007).  $k$ -fold cross-validation is a procedure that estimates prediction error, i.e., how well a model predicts out-of-sample data. The idea is to split the datapoints into  $k$  disjoint groups (called folds). A “validation” fold is left out, and a fit is done with the remaining “training” folds, allowing us to predict the data in the validation fold that was not used in this fitting procedure. This procedure is repeated for all folds. Denoting the datapoints by  $y_i$  and the values predicted on the  $k$ th fold by the cross-validation procedure by

$f_i^{-k}$ , an estimate for the prediction error is

$$\hat{C}V = \frac{1}{N} \sum_{i=1}^N \mathcal{L}(y_i^k - f_i^{-k}),$$

where  $\mathcal{L}(\cdot)$  is the loss function. Examples of loss functions are the  $\mathcal{L}_1$  norm ( $\mathcal{L}_1(x) = |x|$ ) or the  $\mathcal{L}_2$  norm ( $\mathcal{L}_2(x) = x^2$ ).

In our case, the light curves of the  $N$  comparison stars are used to estimate  $l < N$  principal components. These  $l$  principal components, which are a set of light curves  $\{s_i\}_{i=1}^l$ , are our estimates of the systematic effects, and we use the out-of-transit part of the light curve of WASP-6 as the validation data by fitting it with the  $\{s_i\}_{i=1}^l$ . In more precise terms, if  $y(t_k)$  denote the time series of the out-of-transit portion of the light curve of WASP-6, we apply  $k$ -fold cross-validation by considering a model of the form  $y(t_k) = \sum_{i=1}^l \alpha_i s_i(t_k)$ .

#### 4.2. Joint Parameter Estimation for Transit and Stochastic Components

In the past sub-sections we set up an estimation process for the signal given in Equation (2) using PCA. It remains to specify a model for the stochastic signal that we have termed noise, i.e., the  $\epsilon(t)$  term in Equation (1). As noted above, the principal components will absorb part of the  $\epsilon(t)$ , and so our estimate of the noise may not necessarily accurately reflect the  $\epsilon(t)$  term in Equation (1) assuming that the model holds. Nonetheless, this is of no consequence as we just aim to model the residuals after the time series has been modeled with the  $\{s_i\}_{i=1}^l$ . While we still call this term  $\epsilon(t)$  in what follows, one should bear in mind this subtlety. An important feature of the correlated stochastic models we consider is that they can model trends. The  $\{s_i\}_{i=1}^l$  are obtained from the comparison stars, and while the hope is that they capture all of the systematic effects, it is possible that some systematic effects unique to the target star are not captured. The stochastic “noise” models considered below that have time correlations can in principle capture remnant individual trends particular to WASP-6.

We make use of Markov Chain Monte Carlo (MCMC; see, e.g., Ford 2005) algorithms to obtain estimates of the posterior probability distributions of our parameters,  $\theta, \alpha, \eta$ , given a data set  $\mathbf{y}$ , where we have introduced a new set of parameters  $\eta$  characterizing a stochastic component (see below). The posterior distribution  $p(\theta, \alpha, \eta | \mathbf{y})$  is obtained using a prior distribution for our parameters  $p(\theta, \alpha, \eta)$  and a likelihood function,  $p(\mathbf{y} | \theta, \alpha, \eta)$ . Following previous works (e.g., Carter & Winn 2009; Gibson et al. 2012), we assume that the likelihood function is a multivariate Gaussian distribution given by

$$p(\mathbf{y} | \theta, \alpha, \eta) = \frac{1}{(2\pi)^{n/2} |\Sigma_\eta|^{1/2}} \exp \left[ -\frac{1}{2} (\mathbf{y} - \mathbf{g}(\theta, \alpha))^T \times \Sigma_\eta^{-1} (\mathbf{y} - \mathbf{g}(\theta, \alpha)) \right], \quad (4)$$

where  $\mathbf{g}(\theta, \alpha)$  is the function that predicts the observed datapoints and  $\Sigma_\eta$  is the covariance matrix that depends on the set of parameters  $\eta$ . It is the structure of this matrix that defines the type of noise of the residuals. Previous works have proposed to account for time-correlated structure in the residuals using flicker-noise models, where it is assumed that the noise follows a power spectral density (PSD) of the form  $1/f$  (Carter & Winn 2009), and Gaussian processes, where the covariance matrix is

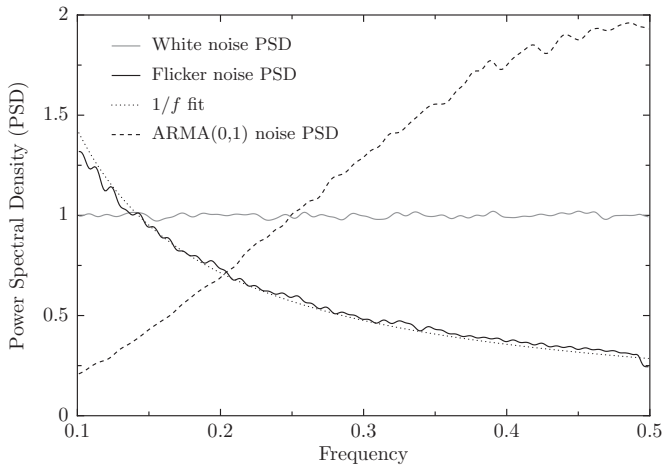


**Figure 3.** Example of the structure that is expected in the power spectral density (PSD) of residual signals of the different types considered in this paper. The PSDs shown here are the mean of 10,000 realizations with the noise structures indicated in the figure. Note that the white-noise PSD is flat, while the flicker-noise and the ARMA(0, 1) models cover low- and high-frequency ranges, respectively.

parametrized with a particular kernel that can incorporate correlations depending on a set of input parameters, including time (Gibson et al. 2012, 2013).<sup>16</sup> In the present work we consider three different models: a white-noise model, where the covariance matrix is assumed to be diagonal; a flicker-noise model; and ARMA( $p, q$ ) models, where the structure of the covariance is determined via the parameters  $p$  and  $q$  (see Section 4.2.2 below for the definition of ARMA( $p, q$ ) models). The reason for choosing these three models is that they sample a wide range of spectral structure of the noise: white-noise models define models where the PSD is flat, while flicker and autoregressive-moving-average (ARMA) like models define noise structures with PSDs with power in low and high frequencies, respectively. Figure 3 illustrates the various structures the PSD can have for the different noise structures considered here.

#### 4.2.1. Flicker Noise Model

Flicker noise is known to arise in many astrophysical time series (Press 1978). It is a type of noise that fits long-range correlations in a stochastic process very well because of its assumed PSD shape of  $1/f$ . An efficient set of algorithms for its implementation in MCMC algorithms was proposed recently by Carter & Winn (2009). The basic idea of this implementation is to assume that the noise is made up of two components: an uncorrelated Gaussian process of constant variance and a correlated Gaussian process that follows this flicker-noise model. These two components are parametrized by  $\sigma_w$  and  $\sigma_r$ , characterizing the white and correlated noise components, respectively. A wavelet transform of the residuals takes the problem into the wavelet basis where flicker noise is nearly uncorrelated, making the problem analytically and computationally more tractable.

<sup>16</sup> In Gibson et al. (2012), a set of optical state parameters is used within a Gaussian process framework to model what we have termed here the perturbation signal, while in Gibson et al. (2013) the Gaussian process is used to account for the time correlation structure of the residuals in a procedure more comparable to ours.

#### 4.2.2. ARMA Noise Model

ARMA models have been in use in the statistical literature for a long time with a very broad range of different applications (Brockwell & Davis 1991). Although known for long in the astronomical community (e.g., Scargle 1981; Koen & Lombard 1993), these noise models have not been used so far for transit light curves to the best of our knowledge.<sup>17</sup>

The time series  $X_{t_k}$  of an ARMA( $p, q$ ) process, where the  $t_k$  are the times of each observation, satisfies

$$X_{t_k} = \sum_{i=1}^p \phi_i X_{t_{k-i}} + \sum_{i=1}^q \theta_i \varepsilon(t_{k-i}) + \varepsilon(t_k), \quad (5)$$

where the  $\{\phi_i\}_{i=1}^p$  and  $\{\theta_i\}_{i=1}^q$  are the parameters of the model and  $\varepsilon_{t_k}$  is white noise with variance  $\sigma_w^2$ . The orders ( $p, q$ ) of the ARMA( $p, q$ ) model define how far in the past a given process looks at when defining future values. Long-range correlations need a high-order ARMA model, while short-range correlations need lower order models. An ARMA model allows us to explore a higher range of noise structures in a complementary way to flicker-noise models.

In order to fit ARMA models to the residuals via an MCMC algorithm, we need the likelihood function of the model given that the residuals follow an ARMA( $p, q$ ) model. For this we implemented the recursive algorithm described in Brockwell & Davis (1991, chapter 8), which assumes that  $\varepsilon(t_k)$  follows a normal distribution with constant variance and that the ARMA process is causal and invertible.

#### 4.2.3. Stochastic Model Selection

Given the three proposed noise models for the stochastic signal  $\varepsilon(t)$ , it remains to define which of the three affords a better description of the data, taking into account the trade-off between the complexity of the proposed model and its goodness of fit. There are several criteria for model selection; a comprehensive comparison between different criteria has been done recently by Vehtari & Ojanen (2012). The main conclusion is that, despite the fact that many model selection criteria have good asymptotic behavior under the constraints that are explicit when deriving them, there is no “perfect model selection” criterion, and there is a need to compare the different methods in the finite-sample case. Following this philosophy, we compare in this work the results of the AIC (“An Information Criterion”; Akaike 1974), the BIC (“Bayesian Information Criterion”; Schwarz 1978), the DIC (“Deviance Information Criterion”; Spiegelhalter et al. 2002), and the DIC<sup>A</sup>, a modified version of DIC with a proposal for bias correction (Ando 2012).

## 5. LIGHT-CURVE ANALYSIS

From the initial 10 comparison stars, only seven were used to correct for systematic effects. One star was eliminated on the grounds of having significantly less flux than the rest, and the other two due to not having the whole spectral range of interest recorded in the CCD. Given the seven comparison stars, we applied PCA to the mean-subtracted time series in order to obtain an estimate of the perturbation signals. We describe now the construction and analysis of the white-light transit light curve and the light curves for 20 wavelength bins.

<sup>17</sup> ARMA( $p, q$ ) models have been considered recently in the modeling of radial velocity data (Tuomi et al. 2013). The very irregular sampling in those data needs careful consideration; in the case of transit light-curve analysis their use is more direct given the nearly uniform sampling that is obtained for these observations.

**Table 2**  
MCMC Priors Used for the White-light Transit Analysis

Transit Parameter	Description	Prior <sup>a</sup>	Units
$R_p/R_s$	Planet-to-star radius ratio	TruncNorm(0.14, 0.01 <sup>2</sup> ) <sup>a</sup>	...
$t_0$	Time of mid-transit	TruncNorm(55473.15, 0.01 <sup>2</sup> ) <sup>b</sup>	MHJD
$P$	Period	TruncNorm(3.36, 0.01 <sup>2</sup> ) <sup>c</sup>	days
$i$	Inclination	TruncNorm(1.546, 0.017 <sup>2</sup> ) <sup>c</sup>	Radians
$R_s/a$	Stellar radius to semi-major axis ratio	TruncNorm(0.09, 0.01 <sup>2</sup> ) <sup>c</sup>	...
$w_1$	Linear limb-darkening coefficient	$U(0, 1)$	...
$\sigma_w$	Standard deviation of the white noise part of the noise model	$U(0, 1)$	mag
$\sigma_r$	Noise parameter for the $1/f$ part of the noise model <sup>d</sup>	$U(0, 1)$	mag

**Notes.**

<sup>a</sup> The TruncNorm( $\mu, \sigma^2$ ) distributions are normal distributions truncated to take values in the range  $(0, \infty)$ , i.e., they are required to be positive. The  $U(a, b)$  distributions are uniform distributions between  $a$  and  $b$ .

<sup>b</sup> Obtained from the values cited in Gillon et al. (2009). The variance of the prior covers more than  $3\sigma$  of their values.

<sup>c</sup> Obtained from the arithmetic mean between the values cited in Gillon et al. (2009) and Dragomir et al. (2011). The variance of the prior covers more than  $3\sigma$  around their values.

<sup>d</sup> Not to be interpreted as the standard deviation of the  $1/f$  part of the noise.

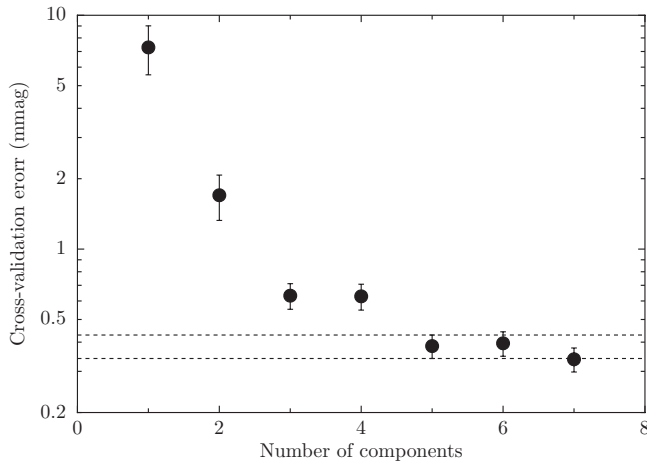


**Figure 4.** Cross-validation error for the prediction of out-of-transit data using a different number of principal components with the 5-fold cross-validation procedure we adopted. Note that the minimum is at  $k = 7$  (dashed lines indicate the value at the minimum and a value higher by  $1\sigma$ ), but the value at  $k = 5$  achieves similar error with lower degrees of freedom.

### 5.1. White-light Transit Light Curve

In order to obtain the white-light transit light curve of WASP-6, we summed the signal over the wavelength range 4718–8879 Å for the target and the comparison stars. Then, we performed 5-fold cross-validation in the out-of-transit part of the light curve of WASP-6 in order to obtain the optimal number of components to be used in our MCMC algorithm. The result of this cross-validation procedure is shown in Figure 4.

From the results of our 5-fold cross-validation procedure one may choose either  $k = 7$  (the value of the minimum error) or  $k = 5$ , which is at less than 1-standard error away from the value at the minimum. We choose this last value because it allows a similar prediction error as the minimum with two less parameter.

Using the first five principal components, we fitted the model proposed in Equation (1) first using a white Gaussian noise model via MCMC using the PyMC python module (Patil et al. 2010). We used wide truncated Gaussian priors<sup>18</sup> in order to incorporate previous measurements of the transit parameters

<sup>18</sup> We denote our truncated Gaussian priors as TruncNorm( $\mu, \sigma^2$ ). They are normal distributions restricted to take values in the range  $(0, \infty)$ , i.e., they are restricted to be positive.

obtained by Gillon et al. (2009) and Dragomir et al. (2011) and the orbital parameters of Gillon et al. (2009). We adopt a quadratic limb-darkening law of the form  $I(\mu) = I(1)[1 - u_1(1 - \mu) - u_2(1 + \mu)^2]$ , where  $\mu = \cos(\theta)$  and  $\{u_1, u_2\}$  are the limb-darkening coefficients. It is well known that  $u_1$  and  $u_2$  are strongly correlated (Pál 2008), and it has been shown that if we define new coefficients ( $w_1, w_2$ ) that are related to  $(u_1, u_2)$  by  $(w_1, w_2) = R(\pi/4)(u_1, u_2)$  where

$$R(\theta) = \begin{pmatrix} \cos(\theta) & -\sin(\theta) \\ \sin(\theta) & \cos(\theta) \end{pmatrix}$$

is a rotation matrix by  $\theta$  radians, then  $w_1, w_2$  are nearly uncorrelated and transits are mostly sensitive to  $w_1$ , with  $w_2$  essentially constant (Howarth 2011). In our MCMC analysis we fix  $w_2$  to the (wavelength dependent) value calculated for the stellar parameters of WASP-6 as described in Sing (2010). Our adopted priors for the white-light transit analysis are detailed in Table 2.

Five MCMC chains of  $10^6$  links each, plus  $10^5$  used for burn-in, were used. We checked that every chain converged to similar values and then thinned the MCMC samples by  $10^4$  in order to get rid of the auto-correlation between the links. We used the thinned sample as our posterior distribution, using the posterior median as an estimate of each parameter (using the point in the chain with the largest likelihood leads to statistically indistinguishable results). The fit using a white Gaussian model for the noise allows us to investigate the structure of the residuals, which show clear long-range correlations, as is evident in the PSD of the residuals plotted in Figure 5. Note that the power is significantly higher at lower frequencies, which suggest that the residuals have long-range correlations. We performed an MCMC fit using a  $1/f$ -like model and another MCMC fit using an ARMA-like model for the residuals. Note that in order to fit an ARMA( $p, q$ ) model with our algorithms, we need to define the order  $p$  and  $q$  of the ARMA process. In order to do this, we fitted several ARMA( $p, q$ ) models to the residuals of the white Gaussian MCMC fit for different orders  $p$  and  $q$  using maximum likelihood and calculated the AIC and BIC of each fit. In the sense of minimizing these information criteria, the “best” ARMA model was an ARMA(2, 2) model, so we performed our MCMC algorithms assuming this as the best model for the ARMA case. The results of the MCMC fits assuming a white Gaussian noise model, an ARMA(2, 2) noise

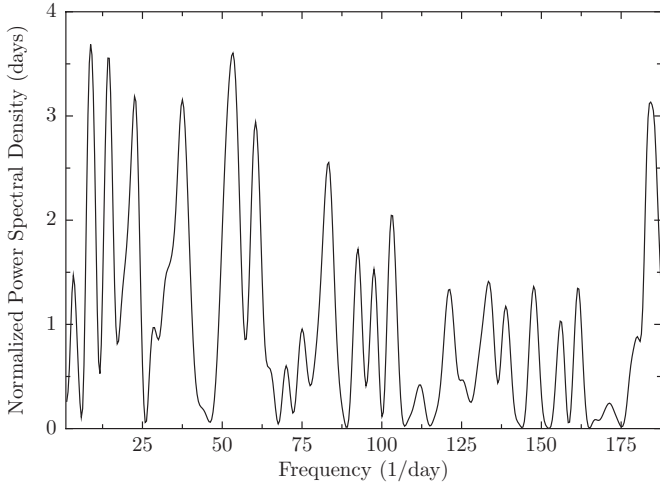


**Figure 5.** Power spectral density of the residuals of the fit using white Gaussian noise (see Figure 6 to see the residuals). Note the preference for high power at small frequencies.

model, and a  $1/f$  noise model for the residuals are shown in Figure 6, and a summary of the values of the information criteria for each of our MCMC fits is shown in Table 3.

It is important to note that the residuals shown in Figure 6 are the signal left over after subtracting the deterministic part of the model only (denoted by  $\mathbf{g}(\theta, \alpha)$  in Equation (4)). Therefore, they still contain, in the case of the ARMA(2, 2) and  $1/f$  noise

**Table 3**  
Values for the Different Information Criteria (IC) for Each Noise Model Considered in Our MCMC Fits

IC	WG Model <sup>a</sup>	ARMA(2, 2) Model <sup>a</sup>	$1/f$ Model <sup>a</sup>
AIC	-1260.59	-1273.38	-1833.72
BIC	-1230.46	-1234.20	-1801.08
DIC	-1165	-1202.03	-1793.60
DIC <sup>A</sup>	-1105.20	-1149.86	-1760.53

**Note.** <sup>a</sup> Note that each of the noise models has a different number of parameters: the white Gaussian noise model (WG model) has 12 parameters, the ARMA(2, 2)-like noise model has 16 parameters, and the  $1/f$ -like noise model has 13 parameters.

models, a correlated stochastic component summed with a white noise component. As opposed to deterministic components, the stochastic components cannot just be predicted given the times  $t_i$  of the observations, as we only know the distribution of expected values once we know the parameters ( $\{\theta_1, \theta_2, \phi_1, \phi_2, \sigma_w\}$  for ARMA(2, 2),  $\{\sigma_r, \sigma_w\}$  for flicker noise, and  $\sigma_w$  for white Gaussian noise). But even though we cannot plot a unique expected trend given the best-fit parameters for the correlated noise models, we can apply filters to the residuals that project them into the best-fit model, or viewed differently, we can filter out the expected white Gaussian noise component, leaving just the correlated part. Such filters allow us then to build *estimates* of the particular realization of a given process that is present in our residuals. For the ARMA(2, 2) and  $1/f$  case we plot in the

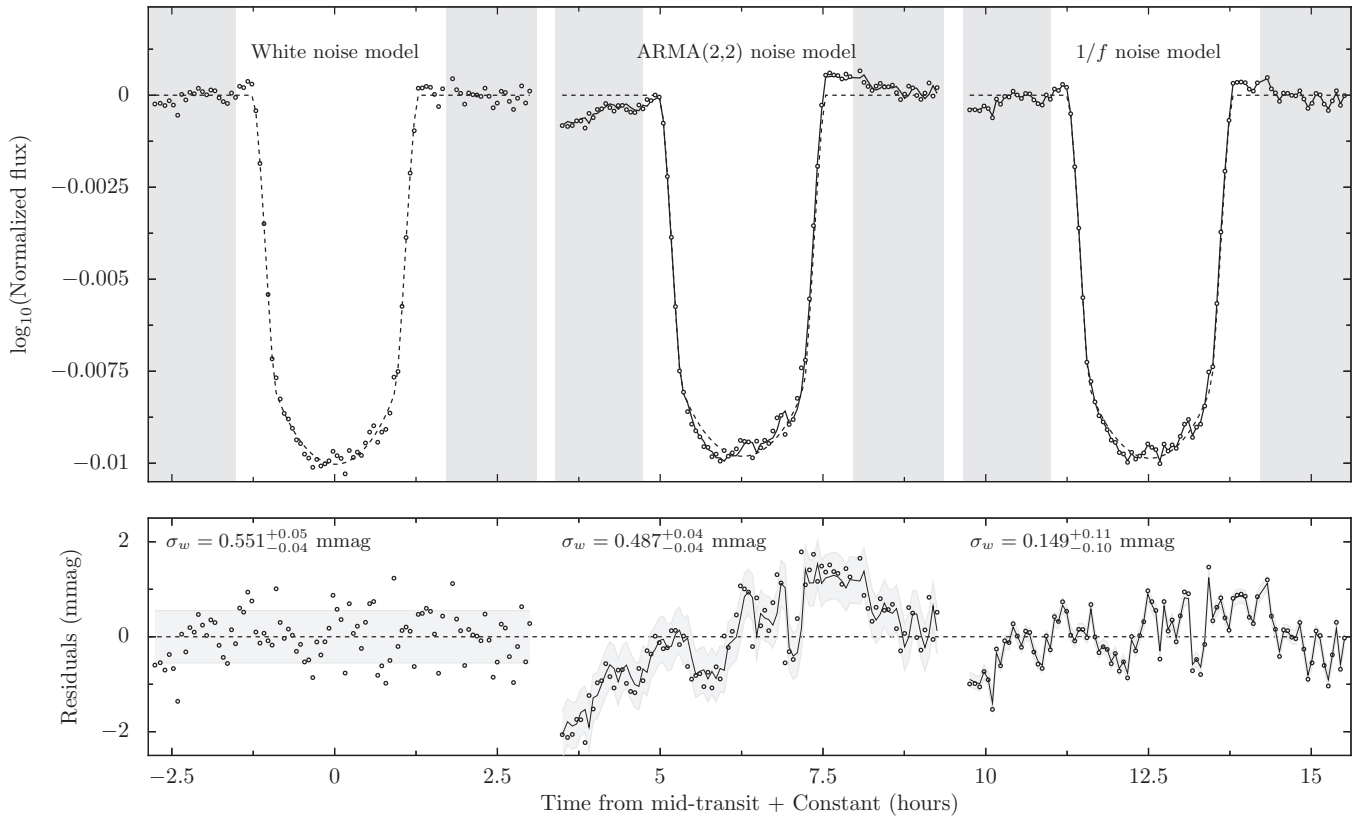


**Figure 6.** Top: the circles show the baseline-subtracted light curves (i.e., light curves with the fitted perturbation signal subtracted) using the different noise models indicated. We also show the corresponding best-fit transit models (dashed line) and the best-fit transit models plus an estimate of the correlated noise component (solid line, only for the two rightmost light curves). The shaded regions indicate points that were used as out-of-transit data by the 5-fold cross-validation procedure that selected the number of principal components to use in the fits. Bottom: residuals between the best-fit transit model and the baseline-subtracted light curves (circles). The solid lines in the two rightmost set of points indicate estimates of the correlated components obtained by projecting the residuals into the best-fit correlated component model (see Section 5). The difference between the points and the solid lines (dashed line for the white Gaussian noise case) is the white Gaussian noise component, whose dispersion  $\sigma_w$  is indicated for each of the noise models considered and also illustrated with  $\pm 1\sigma_w$  bands.

**Table 4**  
WASP-6b Transit Parameters Estimated Using the White-light Transit Light Curve Using a  $1/f$ -like Noise Model

Transit Parameter	Description	Posterior Value	Units
$R_p/R_s$	Planet-to-star radius ratio	$0.1404^{+0.0010}_{-0.0010}$	...
$t_0$	Time of mid-transit	$55473.15365^{+0.00016}_{-0.00016}$	MJD
$P$	Period	$3.3605^{+0.0098}_{-0.0101}$	days
$i$	Inclination	$1.5465^{+0.0074}_{-0.0055}$	Radians
$R_s/a$	Stellar radius to semi-major axis ratio	$0.0932^{+0.0015}_{-0.0015}$	...
$w_1$	Limb-darkening coefficient (see Section 5.1)	$0.44^{+0.12}_{-0.12}$	...
$\sigma_w$	Standard deviation of the white noise part of the noise model	$0.1492^{+0.1078}_{-0.1021}$	mmag
$\sigma_r$	Noise parameter for the $1/f$ part of the noise model <sup>a</sup>	$3.26^{+0.03}_{-0.50}$	mmag

**Note.** <sup>a</sup> Not to be interpreted as the standard deviation of the  $1/f$  part of the noise.

bottom panel of Figure 6 estimates of the correlated components as solid lines through the residuals.<sup>19</sup> It is the difference between these lines and the residual points that constitutes the remaining white Gaussian noise component with dispersion  $\sigma_w$  indicated in the residuals panel.

It is informative to discuss the different values of the  $\sigma_w$  parameter inferred for each of the models we consider. For the white Gaussian noise model, the value of this parameter is  $\sigma_w = 0.55^{+0.05}_{-0.04}$  mmag, which is an order of magnitude higher than the underlying Poisson noise ( $\approx 0.06$  mmag; see Section 2). The same goes for the ARMA-like noise model fit, which has a value for this parameter of  $\sigma_w = 0.49^{+0.04}_{-0.04}$  mmag. Finally, for the  $1/f$ -like noise model the value of this parameter is  $\sigma_w = 0.15^{+0.11}_{-0.10}$  mmag, which is just  $\approx 2.5$  times the Poisson noise limit. Motivated by this result and by the values of the information-theoretic model selection measures quoted in Table 3, we conclude that the preferred model is the one that models the underlying stochastic signal as  $1/f$ -like noise. We note that as Carter & Winn (2009) stress in their work, using this model for the residuals increases the uncertainty in the transit parameter, but provides more realistic estimates for them. We select the model parameters fitted using the  $1/f$  noise model, which are quoted in Table 4, as the best estimates from now on. These parameters are generally an improvement on previous measurements by Gillon et al. (2009) and Dragomir et al. (2011).

We close this section by noting that the principal component regression we adopted was able to recover from the high periods of absorption present 0–2 hr after mid-transit (see Figure 2) without leaving a noticeable trace in the final light curve.

## 5.2. WASP-6b Transmission Spectrum

The procedures explained in the previous sub-section were replicated for the time series of each of 20 wavelength bins, but now leaving only the planet-to-star radius ratio, the linear limb-darkening coefficient  $w_1$ , and the noise parameters as free parameters (all the other transit parameters were fixed to the values shown in Table 4, while the values for  $w_2$  are calculated as indicated in Section 5.1 and are indicated in Table 5). Priors were the same as the white-light analysis for parameters for  $\mu_1$ ,  $\sigma_r$ , and  $\sigma_w$ , and the MCMC chains were set up similarly except that a thinning value of  $10^3$  was used. The prior for  $(R_{pl}/R_*)$  was set to  $\text{TruncNorm}(0.1404, 0.01^2)$ , i.e., we set the mean to the posterior value of our white-light analysis. The wavelength bins were chosen to be  $\approx 200$  Å wide, with

boundaries that lie in the pseudo-continuum of the WASP-6 spectrum, as boundaries in steep parts of the spectrum such as spectral lines would in principle maximize redistribution of flux between adjacent bins under the changing seeing conditions that set the spectral resolution in our setup. For a given spectral bin, the number of principal components was selected separately because different systematics may be dependent on wavelength, and therefore the number of principal components needed may change. In practice, no more than one principal component was added or subtracted in each wavelength bin when compared to the five components used for the white-light curve. In all of them, however, the noise model to be used is the same, the  $1/f$ -like noise model. Figure 7 shows the baseline-subtracted data along with the best-fit transit model at different wavelengths, and Table 5 tabulates the transit parameters from the MCMC analysis for each wavelength bin. The values of  $R_{pl}/R_*$  as a function of wavelength constitute our measured transmission spectrum, which is shown in Figure 8; the typical uncertainty in  $R_{pl}/R_*$  is  $\approx 0.8\%$ , and the inferred  $\sigma_w$  values are typically  $\approx 1$ – $3$  times the Poisson limit in each wavelength bin, for which a typical value is 0.25 mmag.

## 5.3. Limits on the Contribution of Unocculted Stellar Spots

As pointed out in several works (e.g., Pont et al. 2008; Sing et al. 2011b), stellar spots—both occulted and unocculted during transit—can affect the transmission spectrum. In our transit light curve we see no significant deviations that could be attributed to an occulted starspot, so in what follows we estimate the potential signal induced in the transmission spectrum by unocculted stellar spots.

Stellar spots can be modeled as regions in the surface of the star that have a lower effective temperature than the photosphere. Given that WASP-6 is a G star, we can use the Sun as a proxy to infer spot properties. Sunspots can be characterized as having a temperature difference with the photosphere of  $\Delta T \approx -500$  K (Lagrange et al. 2010, see Section 2.2). This is an effective value that represents a good average for the different values of  $\Delta T$  in the umbral and penumbral regions. Given a fraction of the stellar surface  $f_s$  covered by spots characterized by temperature  $T + \Delta T$ , the total brightness of the star will be changed by a factor  $1 + f(\lambda) = 1 + f_s(I_\lambda(T + \Delta T, \theta)/I_\lambda(T, \theta) - 1)$ , where  $I_\lambda(T, \theta)$  is the surface brightness of a star with effective temperature  $T$  and other stellar parameters given by  $\theta = (\log g, Z, \dots)$ . If the fractional change in flux  $\epsilon$  caused by spots at a reference wavelength  $\lambda_0$  can be measured, then  $f_s$  can be inferred to be  $f_s = \epsilon/(I_{\lambda_0}(T + \Delta T, \theta)/I_{\lambda_0}(T, \theta) - 1)$  and we can write

<sup>19</sup> For the  $1/f$  model we use the whitening filter presented in Carter & Winn (2009, see Section 3.4), while for the ARMA(2, 2) process we use prediction equations in the time domain (Brockwell & Davis 1991, see Section 5.1).

**Table 5**  
Transit Parameters as a Function of Wavelength

Wavelength Range (Å)	$(R_p/R_*)$	$w_1$	$w_2^a$	$\sigma_w$ (mmag)	$\sigma_r$ (mmag)	$\sigma_{\text{Poisson}}^b$ (mmag)
4718–4927	0.1430 <sup>+0.0019</sup> <sub>-0.0022</sub>	0.9303 <sup>+0.0523</sup> <sub>-0.1043</sub>	0.2047	0.3048 <sup>+0.2399</sup> <sub>-0.2007</sub>	8.8352 <sup>+0.8051</sup> <sub>-0.8850</sub>	0.31
4927–5115	0.1375 <sup>+0.0016</sup> <sub>-0.0017</sub>	0.8705 <sup>+0.0935</sup> <sub>-0.1616</sub>	0.2016	0.5409 <sup>+0.2104</sup> <sub>-0.2841</sub>	6.5492 <sup>+1.3376</sup> <sub>-1.6895</sub>	0.29
5115–5288	0.1406 <sup>+0.0015</sup> <sub>-0.0016</sub>	0.9127 <sup>+0.0621</sup> <sub>-0.1148</sub>	0.1955	0.7520 <sup>+0.2008</sup> <sub>-0.2591</sub>	5.8071 <sup>+1.9512</sup> <sub>-2.0652</sub>	0.30
5288–5468	0.1400 <sup>+0.0016</sup> <sub>-0.0016</sub>	0.9430 <sup>+0.0427</sup> <sub>-0.0793</sub>	0.2254	0.4151 <sup>+0.1765</sup> <sub>-0.2394</sub>	6.3147 <sup>+0.9081</sup> <sub>-1.1713</sub>	0.27
5468–5647	0.1393 <sup>+0.0009</sup> <sub>-0.0009</sub>	0.8508 <sup>+0.0912</sup> <sub>-0.1080</sub>	0.2326	0.7546 <sup>+0.0771</sup> <sub>-0.1372</sub>	1.8322 <sup>+2.0657</sup> <sub>-1.3047</sub>	0.26
5647–5870	0.1389 <sup>+0.0007</sup> <sub>-0.0007</sub>	0.8114 <sup>+0.0812</sup> <sub>-0.0824</sub>	0.2429	0.6957 <sup>+0.0492</sup> <sub>-0.0465</sub>	0.6417 <sup>+0.7686</sup> <sub>-0.4527</sub>	0.23
5870–6046	0.1392 <sup>+0.0006</sup> <sub>-0.0007</sub>	0.7259 <sup>+0.0866</sup> <sub>-0.0897</sub>	0.2467	0.6109 <sup>+0.0550</sup> <sub>-0.0688</sub>	1.3599 <sup>+1.1107</sup> <sub>-0.9551</sub>	0.25
6046–6269	0.1380 <sup>+0.0005</sup> <sub>-0.0007</sub>	0.4206 <sup>+0.0897</sup> <sub>-0.0831</sub>	0.2477	0.6289 <sup>+0.0512</sup> <sub>-0.0456</sub>	0.6554 <sup>+0.8881</sup> <sub>-0.4690</sub>	0.22
6269–6454	0.1385 <sup>+0.0006</sup> <sub>-0.0006</sub>	0.5400 <sup>+0.0801</sup> <sub>-0.0827</sub>	0.2515	0.6345 <sup>+0.0452</sup> <sub>-0.0441</sub>	0.4624 <sup>+0.6751</sup> <sub>-0.3109</sub>	0.24
6454–6639	0.1390 <sup>+0.0008</sup> <sub>-0.0009</sub>	0.2265 <sup>+0.1195</sup> <sub>-0.1152</sub>	0.2718	0.6525 <sup>+0.0807</sup> <sub>-0.1469</sub>	2.2304 <sup>+1.7794</sup> <sub>-1.6389</sub>	0.24
6639–6830	0.1380 <sup>+0.0012</sup> <sub>-0.0012</sub>	0.5771 <sup>+0.1581</sup> <sub>-0.1621</sub>	0.2526	0.4817 <sup>+0.1580</sup> <sub>-0.2070</sub>	4.5171 <sup>+1.2569</sup> <sub>-1.5051</sub>	0.23
6830–7055	0.1385 <sup>+0.0010</sup> <sub>-0.0012</sub>	0.3163 <sup>+0.1538</sup> <sub>-0.1399</sub>	0.2500	0.5873 <sup>+0.1152</sup> <sub>-0.2005</sub>	2.9911 <sup>+1.8578</sup> <sub>-1.9120</sub>	0.22
7055–7215	0.1373 <sup>+0.0010</sup> <sub>-0.0009</sub>	0.2642 <sup>+0.1219</sup> <sub>-0.1172</sub>	0.2484	0.6105 <sup>+0.0675</sup> <sub>-0.0939</sub>	1.8425 <sup>+1.3572</sup> <sub>-1.1820</sub>	0.27
7215–7415	0.1348 <sup>+0.0010</sup> <sub>-0.0010</sub>	0.1628 <sup>+0.1236</sup> <sub>-0.0973</sub>	0.2481	0.6886 <sup>+0.0561</sup> <sub>-0.0648</sub>	1.0756 <sup>+1.2399</sup> <sub>-0.7853</sub>	0.25
7415–7562	0.1361 <sup>+0.0012</sup> <sub>-0.0011</sub>	0.3190 <sup>+0.1354</sup> <sub>-0.1297</sub>	0.2492	0.6276 <sup>+0.0957</sup> <sub>-0.1215</sub>	2.9063 <sup>+1.2681</sup> <sub>-1.5044</sub>	0.30
7562–7734	0.1359 <sup>+0.0009</sup> <sub>-0.0008</sub>	0.4066 <sup>+0.1013</sup> <sub>-0.0971</sub>	0.2493	0.6145 <sup>+0.0506</sup> <sub>-0.0603</sub>	1.0299 <sup>+1.1571</sup> <sub>-0.7499</sub>	0.31
7734–7988	0.1353 <sup>+0.0009</sup> <sub>-0.0010</sub>	0.3353 <sup>+0.1135</sup> <sub>-0.1066</sub>	0.2494	0.4310 <sup>+0.0654</sup> <sub>-0.0670</sub>	2.1595 <sup>+0.7171</sup> <sub>-0.7261</sub>	0.24
7988–8205	0.1368 <sup>+0.0012</sup> <sub>-0.0012</sub>	0.3408 <sup>+0.1393</sup> <sub>-0.1434</sub>	0.2478	0.3215 <sup>+0.0903</sup> <sub>-0.1173</sub>	3.6847 <sup>+0.6986</sup> <sub>-0.6914</sub>	0.28
8205–8405	0.1391 <sup>+0.0014</sup> <sub>-0.0013</sub>	0.2065 <sup>+0.1626</sup> <sub>-0.1316</sub>	0.2471	0.3888 <sup>+0.1214</sup> <sub>-0.1655</sub>	4.7549 <sup>+0.8495</sup> <sub>-0.9059</sub>	0.31
8405–8630	0.1396 <sup>+0.0012</sup> <sub>-0.0013</sub>	0.2599 <sup>+0.1584</sup> <sub>-0.1405</sub>	0.2454	0.4683 <sup>+0.0991</sup> <sub>-0.1517</sub>	4.4703 <sup>+0.9456</sup> <sub>-0.8350</sub>	0.30

**Notes.**

<sup>a</sup>  $w_2$  is fixed to the values calculated as described in Sing (2010) for the stellar parameters appropriate for WASP-6. Parameters not shown in this table are fixed to the posterior values obtained from the white-light curve analysis shown in Table 4.

<sup>b</sup> Expected Poisson noise level.

$$f(\lambda) = \epsilon(I_\lambda(T + \Delta T, \theta)/I_\lambda(T, \theta) - 1)(I_{\lambda_0}(T + \Delta T, \theta)/I_{\lambda_0}(T, \theta) - 1)^{-1} \text{ (see Sing et al. 2011b, Equation (4)).}$$

A change in the stellar luminosity due to starspots will have an effect on the measured value of  $k = R_p/R_*$ , and as the effect is chromatic, it will induce an effect in the transmission spectrum. The decrease of flux during transit with respect to the out-of-transit flux  $F_0$  is given by  $(\Delta F/F_0) = k^2$  (neglecting any emission from the planet). If  $F_0$  is changed by starspots by a fractional amount  $f(\lambda)$ , we have  $\delta(\Delta F/F_0) \approx -(\Delta F/F_0)\delta F_0/F_0 \equiv -(\Delta F/F_0)f(\lambda) = k^2 f(\lambda) = 2k\delta k$ , where we have used  $f(\lambda) \equiv \delta F_0/F_0$ . From here we get finally<sup>20</sup>

$$\frac{\delta k}{k} = \frac{-f(\lambda)}{2}.$$

We used the method described in Maxted et al. (2011) to look for periodic variations due to spots in the light curves of WASP-6 from the WASP archive (Pollacco et al. 2006). Data from three observing seasons were analyzed independently. The light curves typically contain  $\sim 4500$  observations with a baseline of 200 nights. From the projected equatorial rotation velocity of WASP-6 and its radius (Doyle et al. 2013) we estimate that the rotation period is  $16 \pm 3$  days. There are no significant periodic variations in this range in any of the WASP light curves. To estimate the false alarm probability of any peaks in the periodogram, we use a bootstrap Monte Carlo method. The results of this analysis can also be used to estimate an upper

limit of 2 mmag to the amplitude of any periodic variation in these light curves. Therefore,  $\epsilon$  is constrained to be less than the implied peak-to-peak amplitude,  $|\epsilon| < 4$  mmag. While this constraint is valid only at the time the discovery light curve was taken, lacking any other constraints we will take this value as our upper limit. In order to estimate  $f(\lambda)$ , we make use of the high-resolution Phoenix synthetic stellar spectra computed by Husser et al. (2013). We assume  $T = 5400$  K,  $\Delta T = -500$  K, and other stellar parameters to be the closest available in the model grid to those presented in Gillon et al. (2009). The resulting expected maximum value for  $\delta k/k$  given the constraints on the rotational modulation afforded by the WASP-6 discovery light curve is presented in Figure 9. As can be seen, the change in  $\delta k/k$  induced by starspots over the wavelength range of our spectrum is expected to be  $< 5 \times 10^{-4}$ . This is more than one order of magnitude less than the change in  $\delta k/k$  we infer from our observations (see Figure 8), and thus we conclude that the observed transmission spectrum is not produced by unocculted spots.

## 6. THE TRANSMISSION SPECTRUM: ANALYSIS

The main feature of the transmission spectrum shown in Figure 8 is a general sloping trend with  $R_p/R_*$  becoming smaller for longer wavelengths. The general trend is broken by the two redmost datapoints that could be indicating the presence of a source of opacity in that region, but the error bars of the extreme points are large, as the measurements there are naturally more uncertain because the spectrograph efficiency drops rapidly at the red end of the spectrum and this region of the spectrum can be badly affected by variations in night-sky emission and

<sup>20</sup> This is a special case of the derivation of Désert et al. (2011), namely, their case  $\alpha = -1$ , which corresponds to neglecting changes in brightness of the fraction of the stellar disk that is not affected by spots.

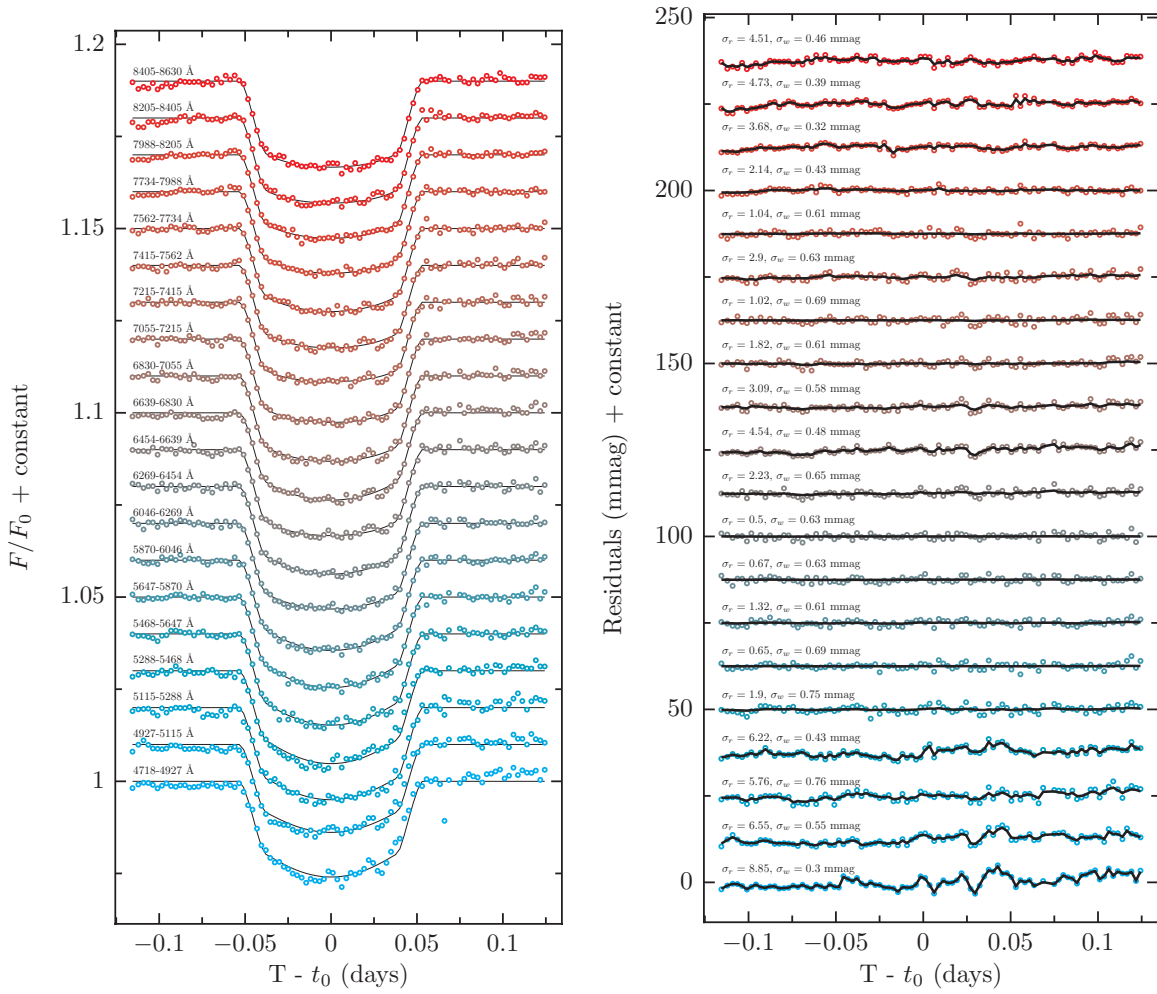


**Figure 7.** Left: transits as observed in different wavelength channels along with the best-fit transit signal plus the stochastic  $1/f$  noise signal. The obvious outlier close to  $t - t_0 = 0.05$  at the first, bluest, wavelength bin was not included in the fit. Right: residuals between the best-fit transit model and the baseline-subtracted light curves for each of the wavelength channels (circles). The solid lines indicate estimates of the correlated  $1/f$  component obtained as described in Section 5. The best-fit parameters of the  $1/f$  component are indicated over each set of residuals.

(A color version of this figure is available in the online journal.)

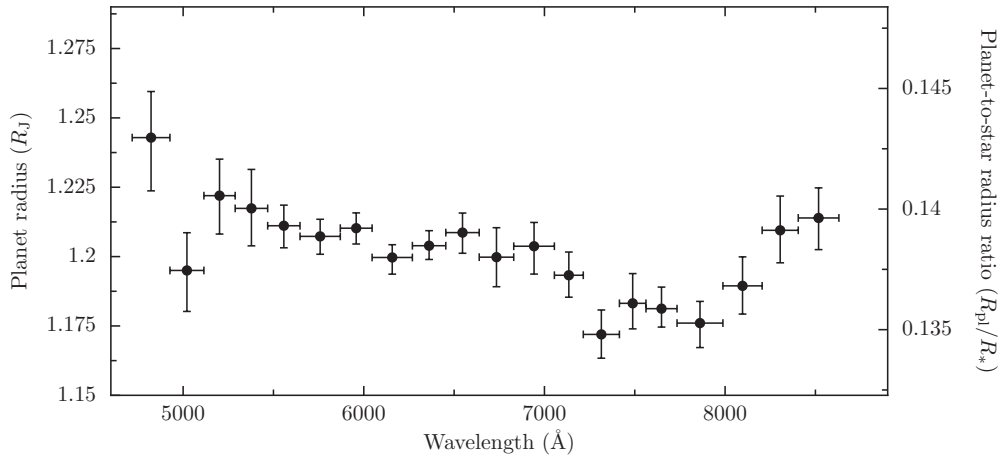


**Figure 8.** Transmission spectrum of WASP-6b measured with IMACS.

telluric absorption. There are no indications of the broad features expected at the resonance doublets of NaI at 589.4 nm or K I at 767 nm. To make the statements above quantitative, we compare our measured transmission spectrum with the clear atmosphere models computed by Fortney et al. (2010).

We scale the models that have a surface gravity of  $g = 10 \text{ m s}^{-2}$  to match the measured surface gravity of WASP-6b ( $g = 8.71 \text{ m s}^{-2}$ ; Gillon et al. 2009) by scaling the spectral features from the base level by  $10/g$ . We do not have an absolute reference to be able to place the 10 bar level such as could be

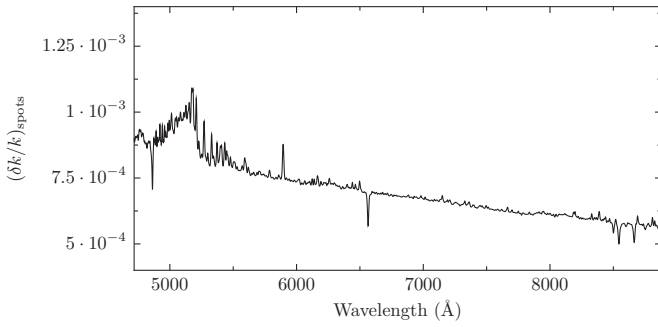


**Figure 9.** Predicted fractional change in  $k = (R_p/R_*)$  due to stellar spots that produce a rotation amplitude of  $\epsilon = -4$  mmag in the V band. The spots are assumed to have a temperature lower than that of the photosphere by  $\Delta T = -500$  K.

provided by observations at infrared wavelengths, which in the Fortney et al. (2010) models is set to  $1.25 R_J$ , and so we fit for an overall offset in the y-axis. In other words, our measured transmission spectrum will be able to discriminate on the shape of the models but will provide no independent information on the absolute height in the atmosphere where the features are formed. Given that the equilibrium planet temperature assuming no albedo and full redistribution between the day and night sides is  $T_{\text{eff}} = 1194^{+58}_{-57}$  K (Gillon et al. 2009), we will compare our measurements with the  $T = 1000$  and  $T = 1500$  K models of Fortney et al. (2010). The  $T = 1000$  K model has Na and K as the main absorbers, while the  $T = 1500$  K model also displays the effects of partially condensed TiO and VO, resulting in very different transmission spectra.

In addition to clear atmosphere models, we fit our data to a pure scattering spectrum as given by Lecavelier Des Etangs et al. (2008) for a scattering cross section  $\sigma = \sigma_0(\lambda/\lambda_0)^\alpha$ ,

$$\frac{d R_p}{d \ln \lambda} = \alpha H_c = \frac{\alpha k_B T}{\mu g}, \quad (6)$$

where  $H_c$  is the scale height of the particles producing the scattering, which we assume to be equal to the gaseous scale height  $H = k_B T/\mu g$ , although condensates producing scattering can have smaller scale heights than the gas,  $H_c \sim H/3$ , unless they are very well mixed vertically (Fortney 2005). In the case of pure scattering we will fit for two parameters to match to our observed spectrum, the combination  $\xi = \alpha T$ , and a zero-point offset. We can then interpret the value of  $\xi$  assuming Rayleigh scattering  $\alpha = -4$  or the expected values of the equilibrium temperature for the atmosphere of WASP-6b.

Along with the transmission spectrum, Figure 10 shows the results of fitting the models to our observed transmission spectrum. It is clear to the eye that the best fit is given by the pure scattering model, with the clear atmosphere models giving considerably worse fits. The clear atmosphere models fail to give a better match to the spectrum due to the lack in the latter of evidence for the broad features expected around Na and K. The AIC for the scattering model assuming Gaussian noise given by the known error bars gives  $-115.3$ , while the values for the  $T = 1000$  and  $T = 1500$  clear atmosphere models are  $-97.2$  and  $-90.9$ , respectively, providing a very significant preference for the scattering model. A  $\chi^2$  analysis gives a  $p$ -value of 0.04 for the pure scattering model ( $\chi^2 = 30$  for 18 degrees of freedom), while the probabilities for the data being produced by either of the clear atmosphere models are exceedingly small ( $\chi^2 = 80$  and 106 with 19 degrees of freedom for the  $T = 1000$  and 1500 models, respectively, giving  $p$ -values  $< 10^{-8}$  for both). Based

on the numbers above, only the scattering model is viable, but these analyses ignore potential correlation of the errors in the wavelength dimension. Looking at the light curves in Figure 7, one can see that in some cases features in the light curves repeat between adjacent wavelength channels. In order to assess the potential impact of correlations in the wavelength direction, we compute the partial autocorrelation function (PACF) for the residuals in the wavelength dimension. Denoting the residuals of the transit fits shown in Figure 7 by  $r_{il}$ , where  $i$  indexes time and  $l$  the wavelength channel, we compute the PACF for the 20 vectors  $(r_{1l}, r_{2l}, \dots, r_{nl})$  with  $l = 1, \dots, 20$  and  $n = 91$ . The PACF has one significant component at lag 1, which shows that the residuals have indeed correlations with the adjacent channels that are suggestive of an AR(1) correlation structure.<sup>21</sup> This does not imply that the  $(R_p/R_*)_\lambda$  values will necessarily have such correlation, but we should check how the models fare when including such potential correlation structure in the fits.

We performed fits then of all three models including an AR(1) component, to see if it gave a significantly better model as gauged by the information criteria listed in Section 4.2.3. The scattering model does not need an additional AR(1) component, while for the clear atmosphere models including correlation gives a significantly better fit. This should come as no surprise, as the clear atmosphere models give a poor fit to start with, and including an extra AR(1) component can effectively model some of the residual structure. But even after accounting for potential correlation structure on them, the scattering model is significantly better than clear atmosphere models. We conclude therefore that our measured transmission spectrum is most consistent with a featureless sloped spectrum and does not present significant evidence for the features predicted by clear atmosphere models even if trying to account for the differences between the model and the observations with correlated errors with short lags between the wavelength channels as suggested by the residuals in the light curves.

The best-fit value for  $\xi$  is  $\xi = -10,670 \pm 3015$ . If we fix the temperature to the equilibrium value given by Gillon et al. (2009), then we would infer  $\alpha = -9 \pm 2.5$ , and, inversely, when assuming Rayleigh scattering we would infer a temperature of  $T = 2667 \pm 750$  K. The inferred values for  $\alpha$  and  $T$  are consistent within  $2\sigma$  from the values for Rayleigh scattering and the equilibrium temperature  $T = 1194^{+58}_{-57}$  given by Gillon et al. (2009), but the uncertainties are too large to allow any further conclusions, especially when considering the additional uncertainty in the scale height assigned to the material responsible for the scattering.

## 7. DISCUSSION AND CONCLUSIONS

We have measured the optical transmission spectrum for WASP-6b in the range  $\approx 480$ – $860$  nm via differential spectrophotometry using seven comparison stars with IMACS on Magellan. By modeling the systematic effects via a PCA of the available comparison stars and a white-noise model for the noise, we are able to achieve light curves with residuals of order  $\approx 0.8$  mmag in 200 nm channels per 140 s exposure, and  $\approx 0.5$  mmag in the summed (white-light) light curve. In order to take into account possible remaining trends particular to the target star and the correlated structure of the noise, we probe the appropriateness of both short (ARMA( $p,q$ )) and long ( $1/f$  “flicker” noise) stochastic processes, making use of well-established information criteria to select the model most

<sup>21</sup> AR( $p$ ) denotes an ARMA( $p,0$ ) process.

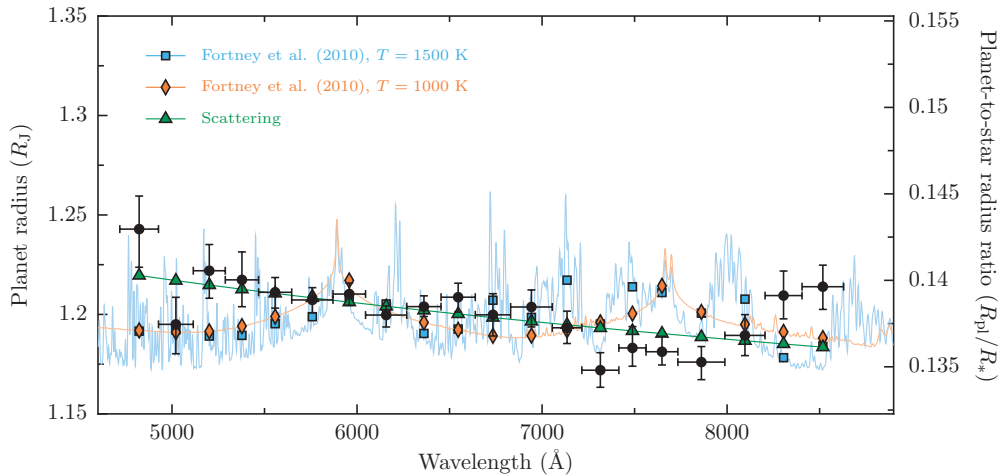


**Figure 10.** Transmission spectrum of WASP-6b along with various models. Black dots with error bars indicate our measurements, while blue squares indicate the binned model of Fortney et al. (2010) with  $T_{\text{eq}} = 1500$  K, and red diamonds indicate the binned model using  $T_{\text{eq}} = 1000$  K. The green line and triangles indicate the best-fit line for a scattering model, which is the favored model in this case.

(A color version of this figure is available in the online journal.)

appropriate for our particular observations, which turned out to be the  $1/f$  model. We believe it is fundamental to carry out a residual analysis for each particular observation. Lacking a detailed physical model for a given correlation structure, it should be the data that select which is the most appropriate for a given observation. With the  $1/f$  model the inferred white noise components are  $\approx 1\text{--}3$  times the expected Poisson shot noise ( $\sigma_w = 0.16$  mmag per 140 s exposure for the white-light curve and  $\sim 0.6$  mmag per 140 s exposure for the 200 nm channels).

The measured spectrum has a general trend of decreasing planetary size with wavelength and does not display any evident additional features. We fit our transmission spectrum with three different models: two clear transmission spectra from Fortney et al. (2010) and a spectrum caused by pure scattering. Our main conclusion is that the transmission spectrum of WASP-6b is most consistent with that expected from a scattering process that is more efficient in the blue. In addition, the spectrum does not show the expected broad features due to alkali metals expected in clear atmosphere models that give significantly less satisfactory description of our data, even when allowing for the errors to be correlated between different wavelength bins.

We conclude that the spectrum is most consistent with a featureless spectrum that can be produced by scattering. The potentially prominent role of condensates or hazes in determining the transmission spectra of exoplanets has been apparent from the very first measurement (Charbonneau et al. 2002), and our transmission spectrum of WASP-6b is in line with what seems to be a building trend for transmission spectra with muted features in the optical. Higher resolution observations around the alkali lines for WASP-6b will be valuable to see whether they remain at detectable levels over the mechanism that is veiling the very broad lines that are expected for clear atmospheres. We note that the expected equilibrium temperature for WASP-6b is similar to that of HD 189733b, so it may be the case that a similar obscurer is acting in both systems.

Our work adds a new instrument (IMACS) to the rapidly increasing set of ground-based facilities that have been successfully used to probe exoplanetary atmospheres. The constraints that can be obtained using ground-based facilities are a powerful complement to those possible from space-based facilities and allow us to access a much broader pool of systems more representative of the typical brightness of hosts discovered by

ground-based transit surveys. An interesting goal enabled by this capability will be to probe the transmission spectra of gas giants with fairly similar surface gravities as a function of equilibrium temperatures.

A.J. acknowledges support from FONDECYT project 1130857, BASAL CATA PFB-06, and the Millennium Science Initiative, Chilean Ministry of Economy (Nucleus P10-022-F). A.J., S.E., and N.E. acknowledge support from the Vicerrectoría de Investigación (VRI), Pontificia Universidad Católica de Chile (proyecto investigación interdisciplinaria 25/2011). N.E. is supported by CONICYT-PCHA/Doctorado Nacional, and M.R. is supported by FONDECYT postdoctoral fellowship 3120097. D.K.S. acknowledges support from STFC consolidated grant ST/J0016/1. J.-M.D. acknowledges funding from NASA through the Sagan Exoplanet Fellowship program administered by the NASA Exoplanet Science Institute (NExScI). A.H.M.J.T. is a Swiss National Science Foundation fellow under grant number PBGEP2-145594.

## REFERENCES

- Akaike, H. 1974, *ITAC*, **19**, 716  
Alonso, R., Brown, T. M., Torres, G., et al. 2004, *ApJL*, **613**, L153  
Ando, T. 2012, *Am. J. Math. Manage. Sci.*, **31**, 13  
Bakos, G., Noyes, R. W., Kovács, G., et al. 2004, *PASP*, **116**, 266  
Bakos, G. Á., Csabry, Z., Penev, K., et al. 2013, *PASP*, **125**, 154  
Bean, J. L., Désert, J.-M., Kabath, P., et al. 2011, *ApJ*, **743**, 92  
Bean, J. L., Désert, J.-M., Seifahrt, A., et al. 2013, *ApJ*, **771**, 108  
Borucki, W. J., Koch, D., Basri, G., et al. 2010, *Sci*, **327**, 977  
Brockwell, P., & Davis, R. 1991, *Time Series: Theory and Methods* (2nd ed., Springer Series in Statistics; Berlin: Springer)  
Brown, T. M. 2001, *ApJ*, **553**, 1006  
Carter, J. A., & Winn, J. N. 2009, *ApJ*, **704**, 51  
Charbonneau, D., Brown, T. M., Noyes, R. W., & Gilliland, R. L. 2002, *ApJ*, **568**, 377  
Colón, K. D., Ford, E. B., Redfield, S., et al. 2012, *MNRAS*, **419**, 2233  
Deming, D., Wilkins, A., McCullough, P., et al. 2013, *ApJ*, **774**, 95  
Désert, J.-M., Sing, D., Vidal-Madjar, A., et al. 2011, *A&A*, **526**, A12  
Doyle, A. P., Smalley, B., Maxted, P. F. L., et al. 2013, *MNRAS*, **428**, 3164  
Dragomir, D., Kane, S. R., Pilyavsky, G., et al. 2011, *AJ*, **142**, 115  
Dressler, A., Bigelow, B., Hare, T., et al. 2011, *PASP*, **123**, 288  
Ford, E. B. 2005, *AJ*, **129**, 1706  
Fortney, J. J. 2005, *MNRAS*, **364**, 649  
Fortney, J. J., Shabram, M., Showman, A. P., et al. 2010, *ApJ*, **709**, 1396  
Gibson, N. P., Aigrain, S., Barstow, J. K., et al. 2013, *MNRAS*, **428**, 3680  
Gibson, N. P., Aigrain, S., Roberts, S., et al. 2012, *MNRAS*, **419**, 2683

- Gillon, M., Anderson, D. R., Triaud, A. H. M. J., et al. 2009, *A&A*, **501**, 785
- Hastie, T., Tibshirani, R., & Friedman, J. 2007, *Elements of Statistical Learning* (2nd ed., Springer Series in Statistics; Berlin: Springer)
- Howarth, I. D. 2011, *MNRAS*, **418**, 1165
- Husser, T.-O., Wende-von Berg, S., Dreizler, S., et al. 2013, *A&A*, **553**, A6
- Jensen, A. G., Redfield, S., Endl, M., et al. 2012, *ApJ*, **751**, 86
- Koen, C., & Lombard, F. 1993, *MNRAS*, **263**, 287
- Lagrange, A.-M., Desort, M., & Meunier, N. 2010, *A&A*, **512**, A38
- Lecavelier Des Etangs, A., Ehrenreich, D., Vidal-Madjar, A., et al. 2010, *A&A*, **514**, A72
- Lecavelier Des Etangs, A., Vidal-Madjar, A., Désert, J.-M., & Sing, D. 2008, *A&A*, **485**, 865
- Mandel, K., & Agol, E. 2002, *ApJL*, **580**, L171
- Marsh, T. R. 1989, *PASP*, **101**, 1032
- Maxted, P. F. L., Anderson, D. R., Collier Cameron, A., et al. 2011, *PASP*, **123**, 547
- McCullough, P. R., Stys, J. E., Valenti, J. A., et al. 2005, *PASP*, **117**, 783
- Pál, A. 2008, *MNRAS*, **390**, 281
- Patil, A., Huard, D., & Fonnesbeck, C. J. 2010, *J. Stat. Softw.*, **35**, 1
- Pepper, J., Pogge, R. W., DePoy, D. L., et al. 2007, *PASP*, **119**, 923
- Pollacco, D. L., Skillen, I., Collier Cameron, A., et al. 2006, *PASP*, **118**, 1407
- Pont, F., Knutson, H., Gilliland, R. L., Moutou, C., & Charbonneau, D. 2008, *MNRAS*, **385**, 109
- Pont, F., Sing, D. K., Gibson, N. P., et al. 2013, *MNRAS*, **432**, 2917
- Press, W. H. 1978, *ComAp*, **7**, 103
- Redfield, S., Endl, M., Cochran, W. D., & Koesterke, L. 2008, *ApJL*, **673**, L87
- Scargle, J. D. 1981, *ApJS*, **45**, 1
- Schwarz, G. 1978, *AnSta*, **6**, 461
- Sing, D. K. 2010, *A&A*, **510**, A21
- Sing, D. K., Désert, J.-M., Fortney, J. J., et al. 2011a, *A&A*, **527**, A73
- Sing, D. K., Huitson, C. M., Lopez-Morales, M., et al. 2012, *MNRAS*, **426**, 1663
- Sing, D. K., Pont, F., Aigrain, S., et al. 2011b, *MNRAS*, **416**, 1443
- Sing, D. K., Vidal-Madjar, A., Désert, J.-M., Lecavelier des Etangs, A., & Ballester, G. 2008, *ApJ*, **686**, 658
- Snellen, I. A. G., Albrecht, S., de Mooij, E. J. W., & Le Poole, R. S. 2008, *A&A*, **487**, 357
- Spiegelhalter, D., Best, N., Carlin, B., & van der Linde, A. 2002, *J. R. Stat. Soc., Ser. B*, **64**, 583
- Tuomi, M., Jones, H. R. A., Jenkins, J. S., et al. 2013, *A&A*, **551**, A79
- Vehtari, A., & Ojanen, J. 2012, *Stat. Surv.*, **6**, 142
- Vidal-Madjar, A., Désert, J.-M., Lecavelier des Etangs, A., et al. 2004, *ApJL*, **604**, L69
- Vidal-Madjar, A., Lecavelier des Etangs, A., Désert, J.-M., et al. 2003, *Natur*, **422**, 143
- Wood, P. L., Maxted, P. F. L., Smalley, B., & Iro, N. 2011, *MNRAS*, **412**, 2376
- Zhou, G., & Bayliss, D. D. R. 2012, *MNRAS*, **426**, 2483